nanomaterials

MDPI

Article

Construction of Hollow Co_3O_4@$ZnIn_2S_4$ p-n Heterojunctions for Highly Efficient Photocatalytic Hydrogen Production

Zijian Xin, Haizhao Zheng and Juncheng Hu *

Hubei Key Laboratory of Catalysis and Materials Science, School of Chemistry and Materials Science, South-Central Minzu University, Wuhan 430074, China

* Correspondence: jchu@mail.scuec.edu.cn; Tel.: +86-27-6784-2752

Abstract: Photocatalysts derived from semiconductor heterojunctions for water splitting have bright prospects in solar energy conversion. Here, a Co_3O_4@ZIS p-n heterojunction was successfully created by developing two-dimensional $ZnIn_2S_4$ on ZIF-67-derived hollow Co_3O_4 nanocages, realizing efficient spatial separation of the electron-hole pair. Moreover, the black hollow structure of Co_3O_4 considerably increases the range of light absorption and the light utilization efficiency of the heterojunction avoids the agglomeration of $ZnIn_2S_4$ nanosheets and further improves the hydrogen generation rate of the material. The obtained Co_3O_4(20) @ZIS showed excellent photocatalytic H_2 activity of 5.38 mmol $g^{-1}\cdot h^{-1}$ under simulated solar light, which was seven times more than that of pure $ZnIn_2S_4$. Therefore, these kinds of constructions of hollow p-n heterojunctions have a positive prospect in solar energy conversion fields.

Keywords: ZIF-67; hollow Co_3O_4 nanocages; $ZnIn_2S_4$ nanosheets; p-n heterojunction; photocatalytic hydrogen production; visible light

check for updates

Citation: Xin, Z.; Zheng, H.; Hu, J. Construction of Hollow Co_3O_4@$ZnIn_2S_4$ p-n Heterojunctions for Highly Efficient Photocatalytic Hydrogen Production. *Nanomaterials* **2023**, *13*, 758. https://doi.org/10.3390/nano13040758

Academic Editors: Jin An Wang, Lifang Chen, Luis Enrique Noreña and Antonino Gulino

Received: 8 January 2023
Revised: 10 February 2023
Accepted: 14 February 2023
Published: 17 February 2023

1. Introduction

The depletion of conventional fossil fuels and the environmental climate issues are forcing people to search for renewable energy [1–5]. Hydrogen, as a renewable energy source, possesses abundant reserves, powerful chemical bonding energy, and environmentally friendly features [6]. For these reasons, photocatalytic hydrogen production from water has attracted widespread attention as an effective way to convert solar energy to clean energy [7]. Honda and Fujishima published ground-breaking research on photoelectrocatalytic water splitting on a TiO_2 electrode in 1974 [8]. Since then, many semiconductor materials have evolved, including metal oxides [9,10], metal sulfides [11], bismuth halides [12,13], and g-C_3N_4. [14]

As one of the typical n-type semiconductor photocatalytic materials, $ZnIn_2S_4$, benefiting from a suitable band gap ($Eg \approx 2.7$ eV) and energy band position, has been widely used in photocatalytic hydrogen production [15]. Furthermore, 2D $ZnIn_2S_4$ nanosheets have the advantages of large specific surface areas and abundant surface-active sites, which facilitate involvement in a wide range of photocatalytic redox reactions (for instance, photocatalytic H_2 evolution, Cr^{VI} reduction, and CO_2 conversion) [16]. But the carrier recombination of single $ZnIn_2S_4$ nanosheets is still severe. They tend to agglomerate into nanospheres, which vastly reduces their specific surface area and the quantity of active sites, and leads to more disordered carrier migration [17,18]. Previous studies have revealed that coupling $ZnIn_2S_4$ with a semiconductor to build a heterojunction can enhance their performance, and mitigate photo corrosion and carrier compounding. Li et al. placed $In(OH)_3$ in sheet planes along the edges of $ZnIn_2S_4$ nanoplates. Under light irradiation, the photocatalytic H_2 evolution performance was about 4.9 times higher compared with pristine $ZnIn_2S_4$, which effectively separates and transfers charges [19]. Liu et al. reported a hybrid photocatalyst prepared by coupling two-dimensional $ZnIn_2S_4$ nanosheets with amino-functionalized

Ti-based MOF [14]. In another study by Zuo and colleagues, sandwich-like hierarchical MXene-$ZnIn_2S_4$ heterostructures were successfully produced by anchoring ultrathin $ZnIn_2S_4$ nanosheets on two surfaces of $Ti_3C_2T_X$MXene [20].

As a member of p-type semiconductors, Co_3O_4 has many advantages, including its strong chemical stability and good electrical, magnetic, and catalytic properties. Thus, Co_3O_4 was used as an oxidative cocatalyst to effectively capture holes generated by the photocatalytic host and promote effective spatial separation of carriers. For instance, Wang and colleagues hydrothermally synthesized 0D/1D TiO_2/Co_3O_4 p-n heterojunctions. The built-in electric field formed in the p-n heterojunctions and Co_3O_4 co-catalyst effect synergistically enhanced carrier transfer and spatial separation [21]. Liu and colleagues made the in situ growth of ZIF-67 onto g-C_3N_4. The p-n heterojunction g-C_3N_4@Co_3O_4 was synthesized by low-temperature sintering. The NO degradation efficiency of the best proportion of the composite sample reached 57% [22]. In addition, the hollow structure has a significant influence the photocatalytic performance.

The hollow structure has drawn increasing attention due to the large surface area and plentiful reactive sites, favoring adsorption activation of the reaction substrate and therefore promoting the redox reaction. Compared with the solid structure, the hollow structure has a thin shell, which makes the carrier transfer pathway shorter and the carrier recombination weaker. The hollow structure can also cause light to be reflected and scattered inside the material, improving light absorption and usage [23–25].

Herein, we successfully fabricated a $ZnIn_2S_4$@Co_3O_4 heterojunction by loading ultrathin two-dimensional $ZnIn_2S_4$ nanosheets onto hollow dodecahedral Co_3O_4 nanocages derived from ZIF-67 by an oil bath. The constructed $ZnIn_2S_4$@Co_3O_4 p-n heterojunction effectively hinders electron-hole recombination. Additionally, the dark hollow structure of Co_3O_4 significantly expands the spectrum of light absorption and the heterojunction's ability to use light efficiently by preventing the accumulation of $ZnIn_2S_4$ nanosheets. Consequently, the optimal $ZnIn_2S_4$@Co_3O_4 composites show apparent enhancement in H_2 production efficiency compared with pure $ZnIn_2S_4$. The $ZnIn_2S_4$@Co_3O_4 heterostructure is stable within 12 h.

2. Experimental Section

2.1. Chemicals and Materials

All chemical reagents used in this experiment were purchased from Sinopharm Chemical Reagent Co., Ltd. (Shanghai, China), which include 2-methylimidazole($C_4H_6N_2$), indium nitrate tetrahydrate ($InCl_3 \cdot 4H_2O$), cobalt nitrate hexahydrate($Co(NO_3)_2 \cdot 6H_2O$), anhydrous zinc chloride ($ZnCl_2$), thioacetamide (C_2H_5NS), glycerol ($C_3H_8O_3$), hydrochloric acid (HCl). All of them were analytical grades, without further purification.

2.2. Synthesis of ZIF-67

First, 2.91 g of $Co(NO_3)_2 \cdot 6H_2O$ and 3.28 g of 2-methylimidazole were dissolved in 200 mL of methanol solution respectively and then the former was slowly poured into the latter with stirring at room temperature for 24 h. The obtained was centrifuged and washed three times with methanol, and then dried overnight at 60° in a vacuum oven.

2.3. Synthesis of Co_3O_4

A certain amount of synthesized ZIF-67 was laid flat in a crucible, placed in a muffle furnace, and calcined at a 2 °C/min rate for 2 h under an air atmosphere.

2.4. Synthesis of $ZnIn_2S_4$@Co_3O_4

A certain amount of as-prepared Co_3O_4 powder was dispersed into the mixture of glycerol (8 mL) and distilled water (32 mL) with the aid of ultrasonication. Then, $ZnCl_2$ (136.3 mg), C_2H_5NS (293.24 mg), and $InCl_3 \cdot 4H_2O$ (293.24 mg) were added into the mixture and ultrasonicated for 5 min and stirred for 25 min. Next, the obtained suspension was transferred into a 100 mL flask and maintained at 80 °C for 2 h. The resultant solid products

were washed with distilled water and ethanol several times and dried at 60 °C. The as-synthesized $ZnIn_2S_4$@Co_3O_4 samples with 10 mg, 20 mg, and 40 mg of Co_3O_4 were labeled as Co_3O_4@ZIS(10), Co_3O_4@ZIS(20), and Co_3O_4@ZIS(40), respectively.

2.5. Characterization

The crystallinity of the samples was investigated by X-ray diffraction (XRD) (Bruker D8 Advance; Cu Kα = 1.5404Å,40 kV, 40 mA;) with a scanning rate of 0.05°/s, using Bragg measurements, and the samples were in powder form, prepared by pressing the slices. The morphologies and sizes of the samples were characterized by SU8010 field-emission scanning electron microscope (FESEM, Hitachi, Japan) with secondary electron measurements. The beam energy was 10μA, and the samples were fixed with liquid conductive adhesive in deceleration mode with an acceleration voltage of 4.5 kV and a landing voltage of 2.0 kV. Transmission electron microscope (TEM) and high-resolution transmission electron microscopy (HRTEM) were measured on a Talos F200X microscope which operated on an accelerating mode of 200 kV. Samples were prepared by crushing and sieving and then dispersed with solvent onto a copper mesh carbon film. The carbon film was then fixed on the sample rod by clamping the carbon film. The measurement methods include bright field, dark field, and HAADF. X-ray photoelectron spectroscopy (XPS) (Thermo Scientific ESCALAB Xi^+) was carried out to analyze the chemical states of the samples. The X-ray source is monochromic Al Kα radiation (hν = 1486.6 eV). The samples were in powder form. Peak deconvolution and spectral analysis were conducted using xpspeak41 software. The background was chosen as smart and the fitted line pattern was L/G Mix. Linewidth differences were relatively subtle. Semiquantitative analysis of elemental content was performed using the Thermo Scientific ESCALAB Xi+ self-contained database, and a corrected Scofield sensitivity factor. The UV–Vis diffused reflectance spectra (DRS) were recorded using a Cary Series UV–Vis–NIR spectrophotometer (Agilent Technologies). Photoluminescence (PL) measurements were characterized on a Hitachi F-7000 with a 150 W Xe lamp.

2.6. Photocatalytic Activities Test

In the photocatalytic activity test system, 20 mg of catalyst was dissolved in a 100 mL aqueous triethanolamine solution (V_{TEOA}:V_{H2O}) and placed in a 400 mL quartz reactor. Then, nitrogen was infused to remove the air from the inner cavity of the reactor for 30 min upon stirring. After the air was exhausted, the reactor was irradiated with a 300 W Xenon lamp equipped with a 420 nm filter simulating visible light, and circulating water was passed through the outer layer of the reactor to avoid the existence of thermal catalysis. After the hydrogen evolution reaction was performed, the nitrogen and hydrogen mixture gas in the 0.4 mL reactor was taken out by the injection needle and taken every 30 min for a total of six times. Hydrogen content was detected by gas chromatography (FULI 9790) equipped with an AE.5A molecular sieve column (3 m × 3 mm) and the oven temperature, thermal conductivity (detector) temperature, and injector temperature of the gas phase are set to 80 °C, 120 °C, and 100 °C, respectively.

2.7. Catalyst Photoelectric Performance Test

In this work, we carried out two photoelectric tests: photocurrent and electrochemical impedance. A three-electrode system and a Chi-760E Chenhua electrochemical workstation are used for the photoelectric test. The three-electrode system used 0.5 mol/L Na_2SO_4 solution as the electrolyte, platinum electrode as the counter electrode, Ag/AgCl electrode as the reference electrode, and ITO conductive glass coated with a layer of the sample as the working electrode.

3. Results and Discussion

At room temperature, Zn^{2+} and 2-methylimidazole synthesize regular dodecahedral ZIF-67 in a methanol solution, which is subsequently placed in a muffle furnace for cal-

cination. The organic ligand in ZIF-67 will undergo oxidation, forming hollow, regular dodecahedrons made of Co_3O_4 particles, and other gases will be liberated. The hollow regular dodecahedron Co_3O_4 will undergo a half-hour ultrasonic stir with sulfur, indium, zinc, and glycerol, followed by a two-hour immersion in oil at 80 °C in a round-bottled flask. This results in the hollow Co_3O_4 surface homogeneous load with extremely thin $ZnIn_2S_4$ heterojunction material.

Figure 1 shows the proposed synthetic method for the p-n heterojunction of $ZnIn_2S_4$@Co_3O_4. ZIF-67 was oxidized into a hollow dodecahedral structure composed of Co_3O_4 particles. Then, the heterojunction material with ultrathin $ZnIn_2S_4$ uniformly loaded on the surface of hollow Co_3O_4 was obtained.

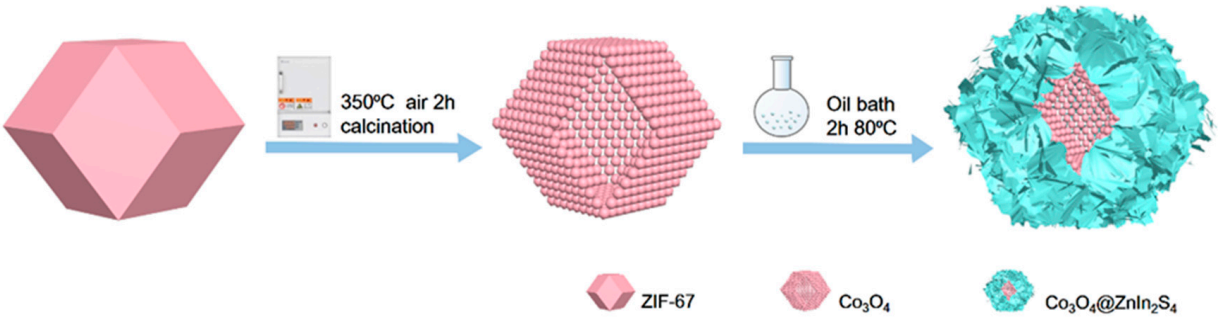

Figure 1. Scheme of the formation of the $ZnIn_2S_4$@Co_3O_4 p-n heterojunction.

XRD is used to analyze the crystal phase structure of materials. As shown in Figure 2a, the precursor ZIF-67 is effectively synthesized, which is compatible with previously published research [26]. In Figure 2b, the peaks of pure Co_3O_4 at 19.05°,31.25°, 36.80°, 44.78°, 59.42°, and 65.24° corresponding to the (111), (220), (311), (222), (511), (440) planes (JCPDS:73-1701) respectively [22]. The positions of the three strong diffraction peaks of $ZnIn_2S_4$ at 21.63°, 27.45°, and 47.49° respectively, correspond to the (006), (102), and (110) crystal planes of $ZnIn_2S_4$ (JCPDS:65-2023) [15]. For Co_3O_4@ZIS, the phase of Co_3O_4 and ZIS are all detected. Compared with the pure sample, they all show the same diffraction peak with no shift, which indicates the successful formation of Co_3O_4@ZIS heterojunction.

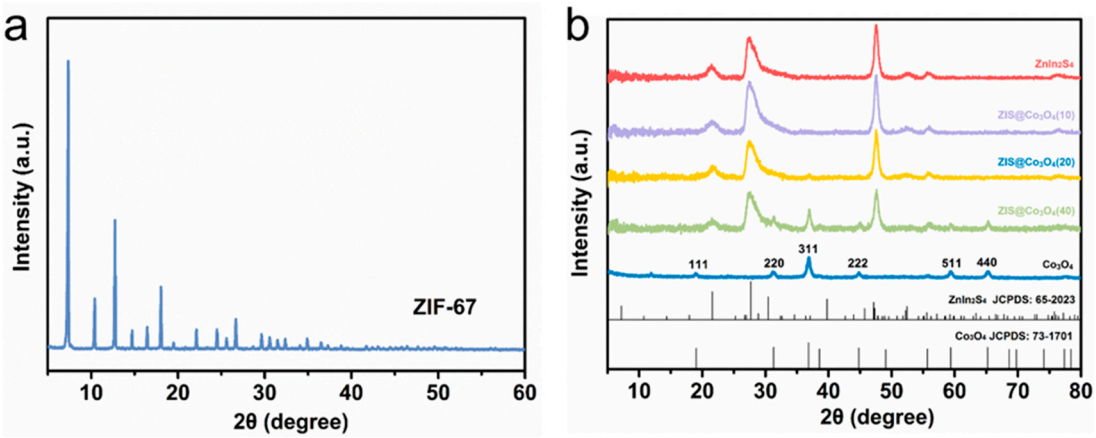

Figure 2. XRD spectra of all samples: (**a**) ZIF-67; (**b**) Co_3O_4, $ZnIn_2S_4$, Co_3O_4(10)@ZIS, Co_3O_4(20)@ZIS, Co_3O_4(40)@ZIS.

The morphology of the obtained resultant products is examined by FE-SEM. A hollow structure of Co_3O_4 with a 500 nm size without collapse and fragmentation in Figure 3(a1–a3) was obtained. The spherical $ZnIn_2S_4$ comprises many sheets with a diameter of about 1 μm. Figure 3(b1–d3) show SEM images of composite samples Co_3O_4 (10) @ ZIS, Co_3O_4 (20) @ ZIS and Co_3O_4 (40) @ ZIS with different proportions, respectively. In terms of surface morphology, these composite samples are spherical, however, the 2D nanosheet arrangement on their

surfaces is more disordered than that of pure $ZnIn_2S_4$ microspheres. The particle sizes of pure $ZnIn_2S_4$ flower-like microspheres are quite different from those of all composite samples, the size of pure $ZnIn_2S_4$ spheroids is about 1μm, and that of composite Co_3O_4 (X) @ ZIS is less than 1 μm (Figure 3(e1–e3)). With the increase of the proportion of Co_3O_4 added in the synthesis process, the particle size of the spherical composite decreases continuously, which probably results from the dispersion of $ZnIn_2S_4$ nanosheets with the same mass on more Co_3O_4 dodecahedron, which causes the decrease in particle size for the spherical composite, indicating the successful construction of heterojunction from the side.

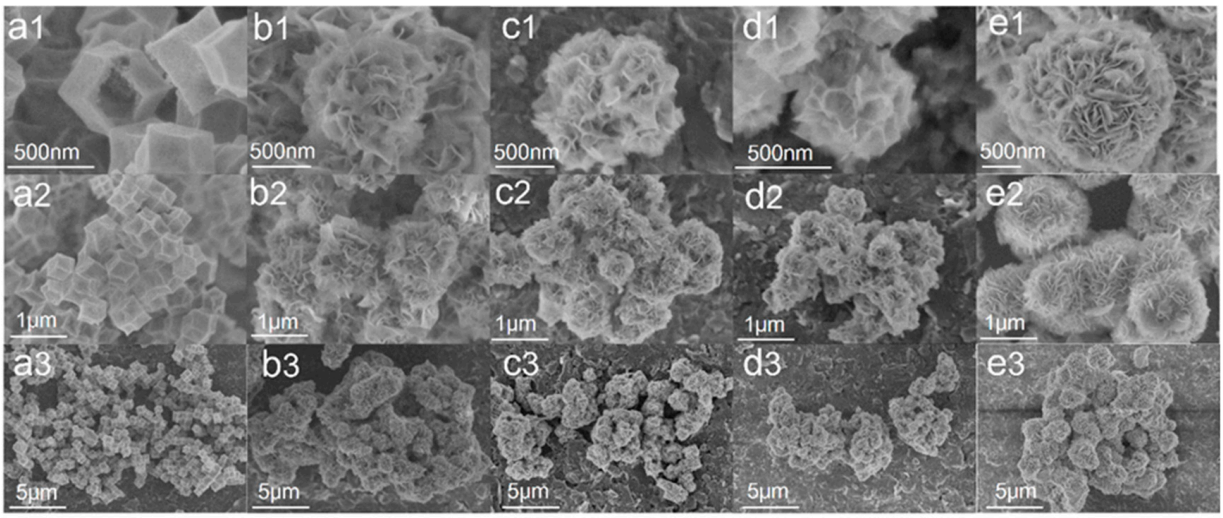

Figure 3. Field emission electron micrographs of all samples at different magnifications: (**a1**–**a3**) Co_3O_4; (**b1**–**b3**) Co_3O_4(10)@ZIS; (**c1**–**c3**) Co_3O_4(20)@ZIS; (**d1**–**d3**) Co_3O_4(40)@ZIS; (**e1**–**e3**) $ZnIn_2S_4$.

The microstructure of the sample is analyzed by STEM. The pure $ZnIn_2S_4$ is a solid flower sphere structure (Figure 4a–c), and the dodecahedral structure of Co_3O_4 is composed of many Co_3O_4 particles Figure 4i–k, which corresponds to the previous SEM results. The hollow structure of Co_3O_4 (20)@ZIS is significantly complete and obvious in Figure 4e–g. Furthermore, in the HRTEM image of $ZnIn_2S_4$ in Figure 4d, lattice distances are 0.190 nm, 0.287 nm, and 0.32 nm, respectively, corresponding to the three crystal planes (110), (104), and (102) of $ZnIn_2S_4$ [27]. Three kinds of lattice fringes of Co_3O_4 were measured. The lattice distances were 0.284 nm, 0.245 nm, and 0.202 nm corresponding to its three crystal planes (220), (311), and (400), respectively [15]. In addition, the HRTEM image of the edge of the Co_3O_4 (20) @ ZIS sample shows that two lattice distances (Figure 4h) are 0.323 nm and 0.283 nm, respectively, corresponding to the (102) and (104) crystal planes of $ZnIn_2S_4$, which proves that $ZnIn_2S_4$ exists in the composite sample. Since Co_3O_4 is completely covered by $ZnIn_2S_4$, the crystal surface of Co_3O_4 cannot be observed.

To further confirm the intimate contact interface element between Co_3O_4 and $ZnIn_2S_4$, the HAADF-STEM-EDX was undertaken. Figure 4m demonstrates the uniformly distributed nature of Zn, S, In, Co, and O. From the element distribution of Co and O, it is apparent that Co_3O_4 is composed of particles, which is consistent with the findings in previous SEM and TEM diagrams. The successful synthesis of the composite sample was further verified.

The X-ray photoelectron spectroscopy (XPS) analysis of the Co_3O_4 @ ZIS, Co_3O_4, and $ZnIn_2S_4$ composites is shown in Figure 5a. As shown in Figure 5b, the Co 2p spectrum is composed of two spin-orbit doublets and two satellite peaks. The binding energies of the first peak in the composite Co_3O_4(20)@ZIS are at 779.70 eV and 781.36 eV, and the second peaks are at 794.28 eV and 796.03 eV, corresponding to the Co $2p_{3/2}$ and Co $2p_{1/2}$ orbitals, respectively, which indicate the coexistence of Co^{2+} and Co^{3+} [28,29]. The high-resolution XPS spectrum of the O element shows three peaks at 529.65 eV, 531.39 eV, and 532.24 eV in Figure 5c. The first and second characteristic peaks correspond to lattice oxygen in metal

oxides and hydroxyl radicals on the surface of materials, while the latter corresponds to adsorbed water on the surface [30–34]. The peaks (Figure 5d) at 1021.73 and 1044.85 eV are attributed to Zn $2p_{3/2}$ and Zn $2p_{1/2}$, respectively, indicating the presence of Zn^{2+} [33]. Figure 5e shows that the two peaks at 444.62 eV and 452.21 eV are assigned to In $3d_{5/2}$In and In $3d_{3/2}$ respectively, indicating that the chemical state of the cation in the composite is plus three [18]. S 2p spectrum (Figure 5f) can be resolved into two peaks including 162.8 and 161.6 eV, corresponding to the S $2p_{1/2}$ and S $2p_{3/2}$ orbitals of S^{2-} [34]. Overall, the XPS results indicate that the binding energies of the Zn, In, and S have a level of red shift compared with pure $ZnIn_2S_4$, which confirms the successful construction of the heterojunction [35].

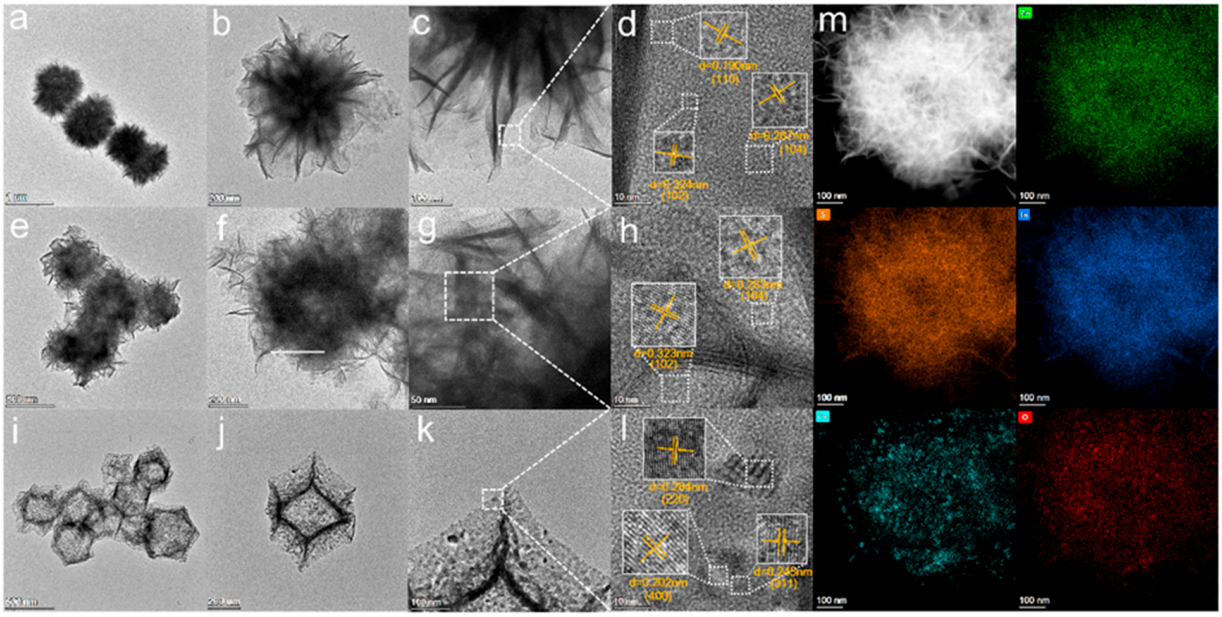

Figure 4. (**a**–**d**) STEM images of $ZnIn_2S_4$ and its HRTEM images; (**e**–**h**) STEM images of Co_3O_4(20)@ZIS and its HRTEM images; (**i**–**l**) STEM images of Co_3O_4 and its HRTEM images; (**m**) HAADF-STEM images of Co_3O_4(20)@ZIS and the corresponding elemental distribution images.

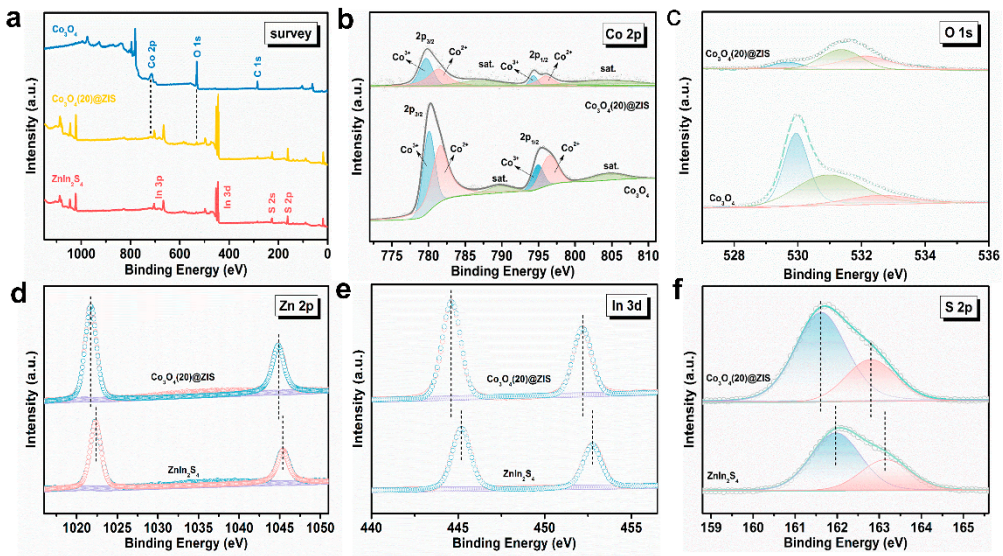

Figure 5. (**a**) General XPS images of Co_3O_4, Co_3O_4(20)@ZIS, and $ZnIn_2S_4$; (**b**) Co 2p;.(**c**) O 1s; (**d**) Zn 2p; (**e**) In 3d; (**f**) S 2p.

The samples' nitrogen adsorption–desorption and pore size distribution curves are shown in Figure 6a–c. Naturally, type IV isotherm and type H3 hysteresis rings are found in all samples, demonstrating the presence of capillary condensation. The materials' microstructure and specific surface area are typically closely connected. As can be observed from the little figure, the three samples all have pore sizes that are mostly spread between 1 and 75 nm, which indicates that they are all mesoporous materials. In Table 1, Co_3O_4(20)@ZIS, $ZnIn_2S_4$, and Co_3O_4 had specific surface area distributions of 121, 15, and 71 $m^2\ g^{-1}$, respectively. Evidently, the specific surface area and pore volume of the Co_3O_4(20)@ZIS composite samples increased with the addition of $ZnIn_2S_4$ in comparison to pure Co_3O_4. It is possible that the composite catalyst will offer more active centers, which will make it easier for photocatalytic hydrogen evolution events to occur. Another angle is that the success of the catalyst preparation is demonstrated by the modification of the adsorption characteristics of the composite samples.

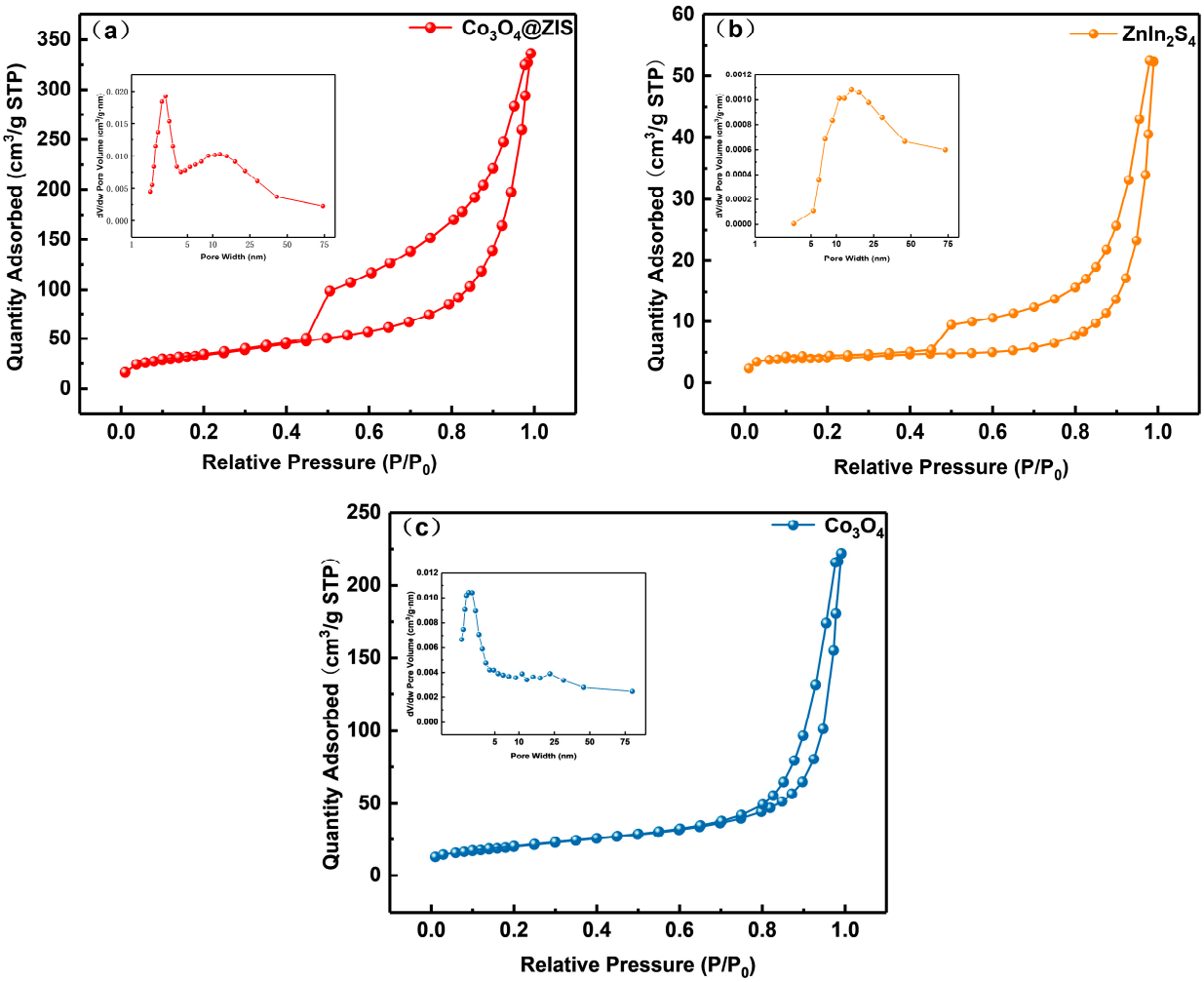

Figure 6. Nitrogen adsorption-desorption isotherms and corresponding pore size distribution curves of (**a**) Co_3O_4(20)@ZIS, (**b**) $ZnIn_2S_4$, and (**c**) Co_3O_4.

Table 1. Adsorption parameters of Co_3O_4(20)@ZIS, $ZnIn_2S_4$ and Co_3O_4.

Sample	S_{BET} ($m^2\ g^{-1}$)	Pore Volume ($cm^3\ g^{-1}$)	Average Pore Size (nm)
Co_3O_4(20)@ZIS	121	0.53	15.39
$ZnIn_2S_4$	15	0.08	31.15
Co_3O_4	71	0.35	19.03

The characterization of phase, morphology, and structure proves the successful synthesis of hollow structure Co_3O_4, and $ZnIn_2S_4$ successfully grows on the surface of Co_3O_4. Based on this point, the hydrogen production performance of all samples is tested under visible light in Figure 7a. Co_3O_4 (20) @ ZIS represents the best ration of the composite sample. Its hydrogen production is as high as 16.14 mmol g^{-1} in three hours, while the hydrogen production performance of pure $ZnIn_2S_4$ is only 2.22 mmol g^{-1}. In addition, the hydrogen production of Co_3O_4 is almost 0 mmol g^{-1}, which may be due to the narrow band gap of Co_3O_4, which causes the carriers to recombine rapidly and prevents them from moving to the surface to take part in the proton reduction process. Figure 7b clearly shows the hydrogen production rate of samples with different proportions, the Co_3O_4 (20) @ ZIS with the best proportion reaches 5.38 mmol g^{-1} L^{-1}. In addition, the hydrogen production rate first rises and then falls with the increase of the proportion of $ZnIn_2S_4$ in the composite sample, which may be due to too much $ZnIn_2S_4$ being loaded onto the surface of the Co_3O_4, thus making the active sites on Co_3O_4 not fully exposed, and resulting in the hole not reacting with sacrificial agents in time, the increase of carrier recombination efficiency, and the decrease of hydrogen production performance [36]. Subsequently, the hydrogen production of Co_3O_4 (20) @ ZIS is tested for a long time to test the stability of the sample. Meanwhile, as shown in Figure 7c and Figure S2, the hydrogen production rate is essentially constant within 12 h, proving the stability of the sample. It also explains that the loading of Co_3O_4 enhances the photocatalytic stability of $ZnIn_2S_4$. Co_3O_4 effectively captures the photo-generated holes produced by the photoexcitation of $ZnIn_2S_4$, which significantly reduces the oxidation process of S^{2-} by holes, and effectively alleviates the photo-corrosion problem of $ZnIn_2S_4$.

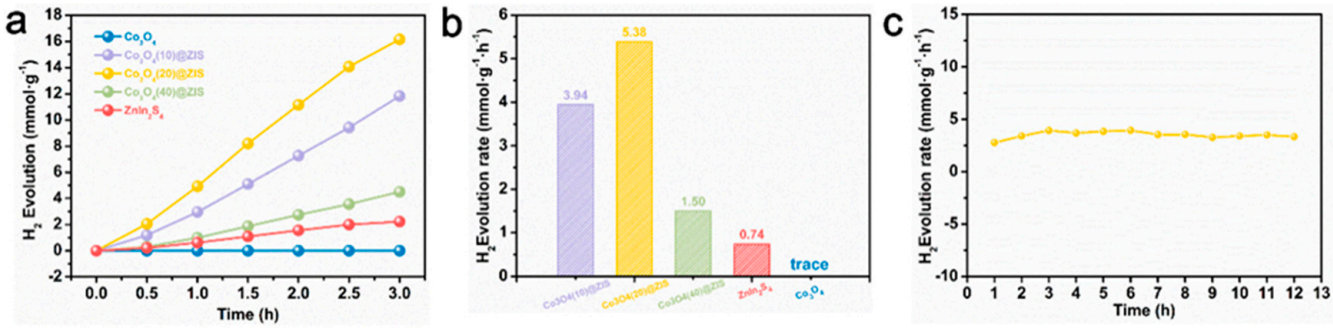

Figure 7. (**a**) Plot of total hydrogen production for each sample; (**b**) Plot of hydrogen production rate for each sample; (**c**) Long time hydrogen production rate of Co_3O_4(20)@ZIS.

To find out the potential reasons for the improved performance of Co_3O_4 (X) @ ZIS, a solid-ultraviolet diffuse reflectance (DRS) test, photoluminescence emission spectrum (PL), photocurrent, electrochemical impedance, and other photoelectrochemical tests are carried out to evaluate the photoelectric performance, carrier separation, and transfer efficiency of the samples. Figure 8a is the solid-ultraviolet diffuse reflectance spectrum (UV-VIS DRS). The absorption range of $ZnIn_2S_4$ is about 510 nm, and Co_3O_4 absorbs in the wavelength range of ultraviolet, visible, and near-infrared light. With the increase of the proportion of Co_3O_4, the absorption range of the composite sample is red-shifted gradually, which corresponds to the color variation of the sample, indicating that $ZnIn_2S_4$ is uniformly loaded on the surface of the Co_3O_4 dodecahedron with a hollow structure and the existence of black Co_3O_4 increases the absorption range and intensity of the sample. According to the formula:

$$\alpha h\nu = A(h\nu - E_g)^{n/2} \quad (1)$$

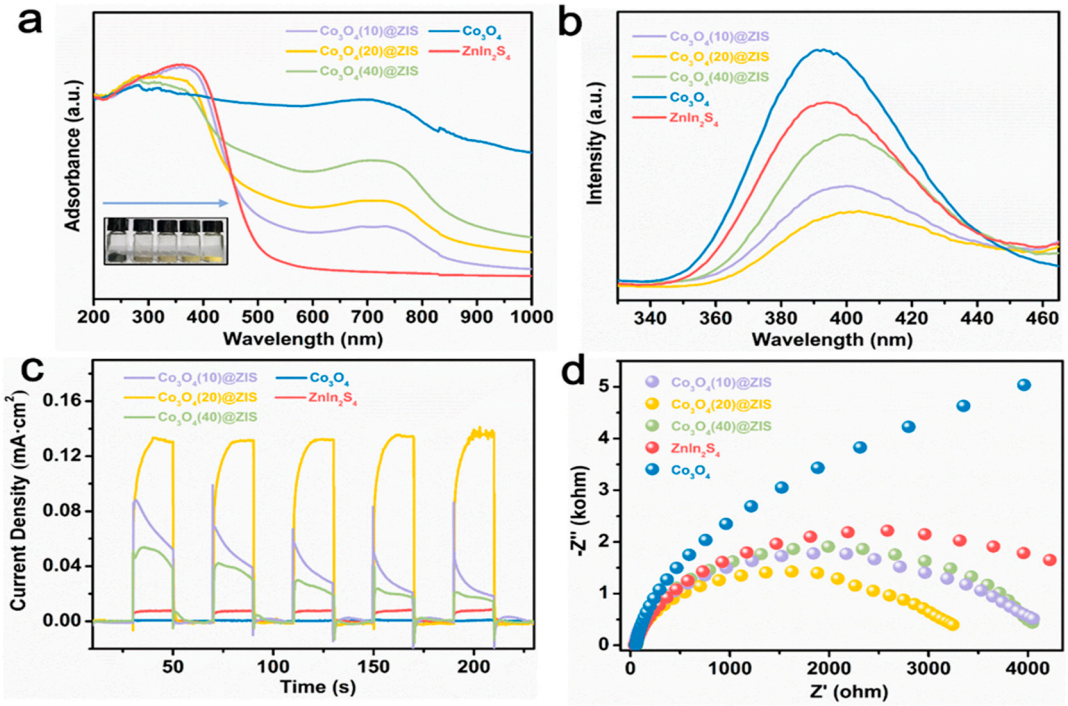

Figure 8. (**a**) DRS plots; (**b**) PL plots; (**c**) photocurrent data; (**d**) EIS data for all samples.

The energy band gaps of Co_3O_4 and $ZnIn_2S_4$ are calculated to be 1.32 eV and 2.70 eV based on the optical absorption band. This result will be helpful to the later energy band mechanism.

Furthermore, Figure 8b is the PL spectra of all the samples, the emission peaks of Co_3O_4 and $ZnIn_2S_4$, and the three composite samples located near 395 nm. Their peak intensities are by Co_3O_4 (20) @ ZIS < Co_3O_4 (10) @ ZIS < Co_3O_4 (40) @ ZIS < $ZnIn_2S_4$, which is consistent with the trend of hydrogen production properties mentioned earlier. The significantly increased separation efficiency of photogenerated electron-hole pairs in the hybrid system is demonstrated by the large quenched PL of all composites compared to Co_3O_4 and $ZnIn_2S_4$.

Transient photocurrent response (TPR) in a classical three-electrode system is used to continue the exploration of the photoelectrochemical characteristics of Co_3O_4 (X) @ ZIS, to understand the potential reasons for the enhanced carrier separating and transfer ability of Co_3O_4 (X) @ ZIS. As shown in Figure 8c, since the black Co_3O_4 has a narrow band gap (Eg = 1.32 eV) and belongs to a narrow band gap transition metal semiconductor, the carrier recombination of Co_3O_4 is too fast, resulting in no photocurrent signal or its weak signal. Meanwhile, it is found that pure $ZnIn_2S_4$ nanospheres exhibit a small photocurrent intensity due to the corrosion of ternary sulfide and serious carrier recombination caused by the solid structure. As anticipated, after loading $ZnIn_2S_4$ onto the hollow nanostructure of Co_3O_4, the photocurrent intensity of the composite sample was significantly higher than that of the two substrates. Among all the composite samples, Co_3O_4 (20) @ ZIS has the strongest photocurrent signal, indicating that Co_3O_4 in the heterojunction system can make $ZnIn_2S_4$ carriers excited under visible light separate and migrate rapidly. The transfer impedance of photoexcited carriers in the heterojunction is observed via electrochemical impedance spectroscopy (EIS). As shown in Figure 8d, the semicircle formed by the Nernst curve of Co_3O_4 (20) @ ZIS is the smallest semicircle in the produced samples, offering the lowest transfer impedance during photocatalytic activity [37,38]. It is in perfect agreement with the photocurrent test and fluorescence test.

Mott–Schottky tests were performed to analyze the energy band structure of Co_3O_4 and $ZnIn_2S_4$, and reasonable assumptions were made on the catalytic mechanism of catalyst materials based on the energy band structure (Figure 9). According to the formula:

$$\frac{1}{C^2} = \frac{2}{\varepsilon\varepsilon_0 e N_D}\left(V - V_{FB} - \frac{K_B T}{e}\right) \quad (2)$$

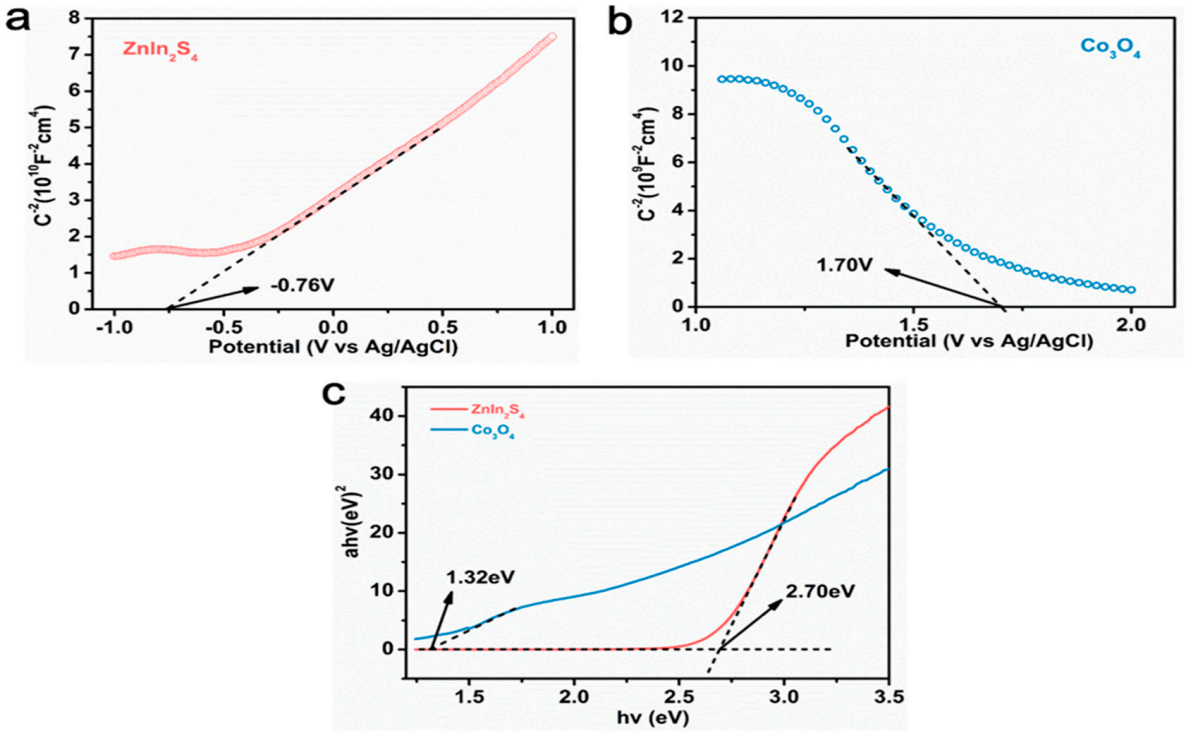

Figure 9. (**a**,**b**) The Mott-Schottky curve of $ZnIn_2S_4$ and Co_3O_4;(**c**) The band gap of $ZnIn_2S_4$ and Co_3O_4.

The Mott–Schottky curve of $ZnIn_2S_4$, in which the slope of the linear part is positive, indicates that $ZnIn_2S_4$ is an n-type semiconductor, and the flat band potential (E_{fb}) is −0.54 eV (−0.76 eV vs. Ag/AgCl), relative to the standard hydrogen electrode. Figure 9b shows the Mott–Schottky curve of Co_3O_4, in which the slope of the linear part is negative, indicating that Co_3O_4 is a p-type semiconductor, and the flat band potential (E_{fb}) is 1.92 eV (1.70 vs. Ag/AgCl) relative to the standard hydrogen electrode. According to earlier findings, the conduction band value for n-type semiconductors is 0.1 eV lower than the flat-band potential, while the valence band value for p-type semiconductors is 0.1 eV higher than the flat-band potential, resulting in ECB ($ZnIn_2S_4$) =−0.64 eV and EVB (Co_3O_4) = 2.02 eV. In conjunction with the band gap values determined using the DRS pattern from the prior research, as shown in Figure 9c, Eg ($ZnIn_2S_4$) = 2.70 eV and Eg (Co_3O_4) = 1.32 eV, it can be calculated that EVB ($ZnIn_2S_4$) =−2.06 eV and ECB (Co_3O_4) = 0.70 eV. This energy band structure promotes the formation of Co_3O_4 (X) @ ZIS p-n heterojunction.

The mechanism hypothesis of Co_3O_4 (X) @ $ZnIn_2S_4$ heterojunction participating in photocatalytic hydrogen production is shown in Figure 10. Before the Co_3O_4 and $ZnIn_2S_4$ contact, $ZnIn_2S_4$ has a higher Fermi level (Ef) than Co_3O_4. When $ZnIn_2S_4$ is loaded on Co_3O_4, a close contact surface will be formed between them. The negative charge in $ZnIn_2S_4$ is transferred to Co_3O_4 through the interface, and the positive charge in Co_3O_4 is transferred to $ZnIn_2S_4$ through the interface until their Fermi levels are equal, and a built-in electric field from $ZnIn_2S_4$ to Co_3O_4 is formed. It is worth mentioning that the energy band positions of the two will also move with the Fermi level, and the conduction band of Co_3O_4 will move to a more negative position than that of $ZnIn_2S_4$ so that electrons

on the Co_3O_4 conduction band can transfer to $ZnIn_2S_4$ conduction band. However, the built-in electric field can further guide the electron transfer from the conduction band of p-type semiconductor Co_3O_4 to the conduction band of $ZnIn_2S_4$, and the hole transfer from the valence band of n-$ZnIn_2S_4$ to the valence band of Co_3O_4, which promotes the spatial separation of electron-hole pairs. Therefore, more electrons are transferred to $ZnIn_2S_4$ nanosheets and participate in the proton reduction reaction.

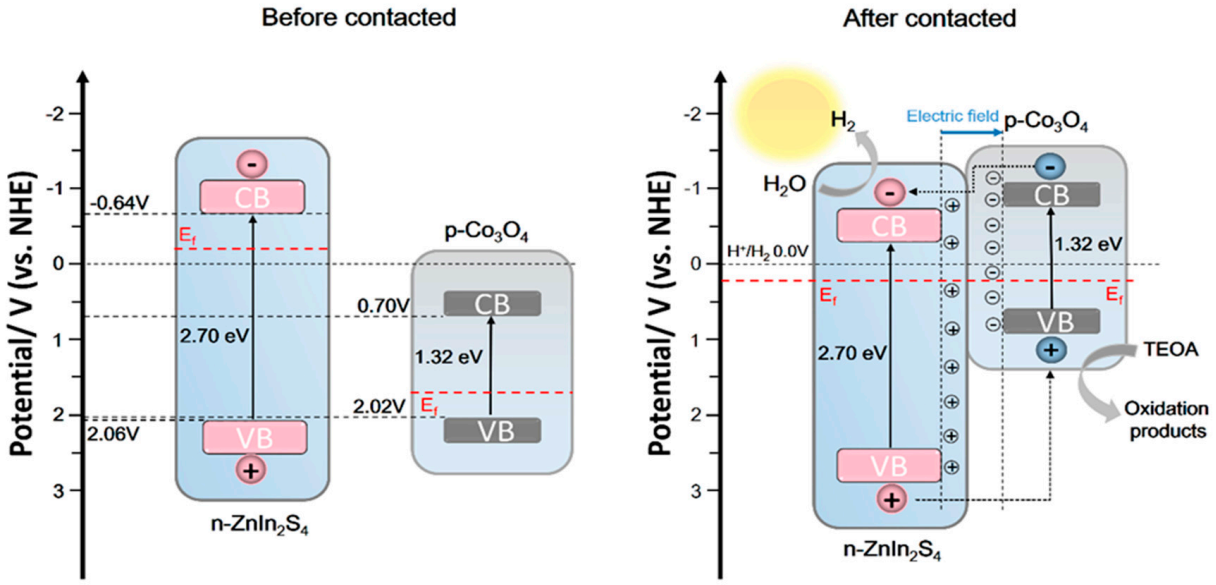

Figure 10. Mechanism of photocatalytic hydrogen production from Co_3O_4(X)@$ZnIn_2S_4$ p-n heterojunction.

4. Conclusions

The nanocomposite Co_3O_4@ $ZnIn_2S_4$ with intimate contact was synthesized by the mild oil bath. The p-n heterojunctions were successfully constructed, forming the internal electric field and effectively realizing spatial separation of carriers. Moreover, Co_3O_4 broadened the absorbance range and enhanced the absorbance intensity of the composite Co_3O_4@ $ZnIn_2S_4$ in this hybridized system. Furthermore, the hollow structure of Co_3O_4 further improved the utilization rate of light. As a result, the optimal Co_3O_4 (20)@ $ZnIn_2S_4$ photocatalyst exhibited an H_2 evolution rate of 5.38 mmol·g^{-1}·L^{-1}. this rate is seven times higher than that of pure $ZnIn_2S_4$. Therefore, this work offers some helpful advice for the development of hollow p-n heterojunctions in the future and their utilization in the area of energy conversion.

Supplementary Materials: The following supporting information can be downloaded at: https://www.mdpi.com/article/10.3390/nano13040758/s1, Table S1: Comparison with other catalysts; Figure S1: TG results of the Co_3O_4(20)@ZIS; Figure S2: Three cycles of experiment of the Co_3O_4(20)@ZIS. References [18,39–44] are cited in Supplementary Materials.

Author Contributions: Conceptualization, Z.X.; H.Z. and J.H.; investigation, Z.X. and H.Z.; writing—original draft preparation, Z.X. and H.Z.; writing—review and editing, Z.X. and H.Z.; supervision, J.H. All authors have read and agreed to the published version of the manuscript.

Funding: This work was financially supported by the National Natural Science Foundation of China (22272207, 21673300) and Fundamental Research Funds for the Central Universities, China (CZT19001).

Conflicts of Interest: The authors declare no competing financial interests.

References

1. Wang, X.; Zhao, Y.; Mølhave, K.; Sun, H. Engineering the Surface/Interface Structures of Titanium Dioxide Micro and Nano Architectures towards Environmental and Electrochemical Applications. *Nanomaterials* **2017**, *7*, 382. [CrossRef] [PubMed]
2. Yadav, A.A.; Hunge, Y.M.; Kang, S.-W. Visible Light-Responsive CeO_2/MoS_2 Composite for Photocatalytic Hydrogen Production. *Catalysts* **2022**, *12*, 1185. [CrossRef]
3. Hunge, Y.M.; Yadav, A.A.; Kang, S.-W.; Lim, S.J.; Kim, H. Visible light activated MoS_2/ZnO composites for photocatalytic degradation of ciprofloxacin antibiotic and hydrogen production. *J. Photochem. Photobiol. A Chem.* **2023**, *434*, 114250. [CrossRef]
4. Hunge, Y.M.; Yadav, A.A.; Kang, S.W.; Kim, H. Facile synthesis of multitasking composite of Silver nanoparticle with Zinc oxide for 4-nitrophenol reduction, photocatalytic hydrogen production, and 4-chlorophenol degradatio. *J. Alloys Compd.* **2022**, *928*, 167133. [CrossRef]
5. Yadav, A.A.; Hunge, Y.M.; Kang, S.W. Spongy ball-like copper oxide nanostructure modified by reduced graphene oxide for enhanced photocatalytic hydrogen production. *Mater. Res. Bull.* **2021**, *133*, 111026. [CrossRef]
6. Wang, Z.; Li, C.; Domen, K. Recent developments in heterogeneous photocatalysts for solar-driven overall water splitting. *Chem. Soc. Rev.* **2019**, *48*, 2109–2125. [CrossRef]
7. Yuan, Y.-J.; Chen, D.; Yu, Z.-T.; Zou, Z.-G. Cadmium sulfide-based nanomaterials for photocatalytic hydrogen production. *J. Mater. Chem. A* **2018**, *6*, 11606–11630. [CrossRef]
8. Fujishima, A.; Honda, K. Electrochemical Photolysis of Water at a Semiconductor Electrode. *Nature* **1972**, *238*, 37–38. [CrossRef]
9. Xie, M.; Dai, X.; Meng, S.; Fu, X.; Chen, S. Selective oxidation of aromatic alcohols to corresponding aromatic aldehydes using In_2S_3 microsphere catalyst under visible light irradiation. *Chem. Eng. J.* **2014**, *245*, 107–116. [CrossRef]
10. Poudel, M.B.; Lohani, P.C.; Kim, A.A. Synthesis of silver nanoparticles decorated tungsten oxide nanorods as high-performance supercapacitor electrode. *Chem. Phys. Lett.* **2022**, *804*, 139884. [CrossRef]
11. Poudel, M.B.; Kim, A.R.; Ramakrishan, S. Integrating the essence of metal organic framework-derived ZnCoTe–N–C/MoS_2 cathode and ZnCo-NPS-N-CNT as anode for high-energy density hybrid supercapacitors. *Compos. Part B-Eng.* **2022**, *247*, 110339. [CrossRef]
12. Shi, Y.; Xiong, X.; Ding, S.; Liu, X.; Jiang, Q.; Hu, J. In-Situ topotactic synthesis and photocatalytic activity of plate-like BiOCl/2D networks Bi_2S_3 heterostructures. *Appl. Catal. B-Environ.* **2018**, *220*, 570–580. [CrossRef]
13. Xiong, X.; Zhou, T.; Liu, X.; Ding, S.; Hu, J. Surfactant-mediated synthesis of single-crystalline Bi_3O_4Br nanorings with enhanced photocatalytic activity. *J. Mater. Chem. A* **2017**, *5*, 15706–15713. [CrossRef]
14. Dong, J.; Zhang, Y.; Hussain, M.I.; Zhou, W.; Chen, Y.; Wang, L.-N. g-C_3N_4: Properties, Pore Modifications, and Photocatalytic Applications. *Nanomaterials* **2022**, *12*, 121. [CrossRef]
15. Zhang, E.; Zhu, Q.; Huang, J.; Liu, J.; Tan, G.; Sun, C.; Li, T.; Liu, S.; Li, Y.; Wang, H.; et al. Visually resolving the direct Z-scheme heterojunction in CdS@$ZnIn_2S_4$ hollow cubes for photocatalytic evolution of H_2 and H_2O_2 from pure water. *Appl. Catal. B-Environ.* **2021**, *293*, 120213. [CrossRef]
16. Tang, B.; Yu, Z.G.; Zhang, Y.; Tang, C.; Seng, H.L.; Seh, Z.W.; Zhang, Y.-W.; Pennycook, S.J.; Gong, H.; Yang, W. Metal–organic framework-derived hierarchical MoS_2/CoS_2 nanotube arrays as pH-universal electrocatalysts for efficient hydrogen evolution. *J. Mater. Chem. A* **2019**, *7*, 13339–13346. [CrossRef]
17. Peng, X.; Ye, L.; Ding, Y.; Yi, L.; Zhang, C.; Wen, Z. Nanohybrid photocatalysts with $ZnIn_2S_4$ nanosheets encapsulated UiO-66 octahedral nanoparticles for visible-light-driven hydrogen generation. *Appl. Catal. B-Environ.* **2020**, *260*, 118152. [CrossRef]
18. Liu, H.; Zhang, J.; Ao, D. Construction of heterostructured $ZnIn_2S_4$@NH_2-MIL-125(Ti) nanocomposites for visible-light-driven H_2 production. *Appl. Catal. B-Environ.* **2018**, *221*, 433–442. [CrossRef]
19. Li, Y.; Hou, Y.; Fu, Q.; Peng, S.; Hu, Y.H. Oriented growth of $ZnIn_2S_4/In(OH)_3$ heterojunction by a facile hydrothermal transformation for efficient photocatalytic H_2 production. *Appl. Catal. B-Environ.* **2017**, *206*, 726–733. [CrossRef]
20. Zuo, G.; Wang, Y.; Teo, W.L.; Xie, A.; Guo, Y.; Dai, Y.; Zhou, W.; Jana, D.; Xian, Q.; Dong, W.; et al. Ultrathin $ZnIn_2S_4$ Nanosheets Anchored on Ti_3C_2TX MXene for Photocatalytic H_2 Evolution. *Angew. Chem. Int. Ed.* **2020**, *59*, 11287–11292. [CrossRef] [PubMed]
21. Wang, L.; Tang, G.; Liu, S.; Dong, H.; Liu, Q.; Sun, J.; Tang, H. Interfacial active-site-rich 0D Co_3O_4/1D TiO_2 p-n heterojunction for enhanced photocatalytic hydrogen evolution. *Chem. Eng. J.* **2022**, *428*, 131338. [CrossRef]
22. Liu, D.; Chen, D.; Li, N.; Xu, Q.; Li, H.; He, J.; Lu, J. ZIF-67-Derived 3D Hollow Mesoporous Crystalline Co_3O_4 Wrapped by 2D g-C_3N_4 Nanosheets for Photocatalytic Removal of Nitric Oxide. *Small* **2019**, *15*, 1902291. [CrossRef] [PubMed]
23. Lai, X.; Li, J.; Korgel, B.A.; Dong, Z.; Li, Z.; Su, F.; Du, J.; Wang, D. General Synthesis and Gas-Sensing Properties of Multiple-Shell Metal Oxide Hollow Microspheres. *Angew. Chem.-Int. Edit.* **2011**, *50*, 2738–2741. [CrossRef] [PubMed]
24. Sun, J.; Zhang, J.; Zhang, M.; Antonietti, M.; Fu, X.; Wang, X. Bioinspired hollow semiconductor nanospheres as photosynthetic nanoparticles. *Nat. Commun.* **2012**, *3*, 1139. [CrossRef]
25. Xing, F.; Liu, Q.; Huang, C. Mo-Doped $ZnIn_2S_4$ Flower-Like Hollow Microspheres for Improved Visible Light-Driven Hydrogen Evolution. *Sol. RRL* **2020**, *4*, 1900483. [CrossRef]
26. Chang, N.; Chen, Y.-R.; Xie, F.; Liu, Y.-P.; Wang, H.-T. A promising Z-scheme heterojunction via loading Ag/AgCl into porous Co_3O_4 derived from ZIF-67 for visible light driven photocatalysis. *Microporous Mesoporous Mat.* **2020**, *307*, 110530. [CrossRef]
27. Zhang, X.; Ding, S.; Luo, X.; Huang, C.; Dong, T.; Yang, Y.; Liu, N.; Hu, J. Engineering amorphous red phosphorus onto $ZnIn_2S_4$ hollow microspheres with enhanced photocatalytic activity. *Mater. Lett.* **2018**, *232*, 78–81. [CrossRef]

28. Zhang, G.; Chen, D.; Li, N.; Xu, Q.; Li, H.; He, J.; Lu, J. Construction of Hierarchical Hollow $Co_9S_8/ZnIn_2S_4$ Tubular Heterostructures for Highly Efficient Solar Energy Conversion and Environmental Remediation. *Angew. Chem.-Int. Edit.* **2020**, *59*, 8255–8261. [CrossRef]
29. Syed, A.; Elgorban, A.M.; Bahkali, A.H.; Zaghloul, N.S.S. Coupling of nano-spinel $MgFe_2O_4$ on Co_3O_4 for heterogeneous photocatalysis and antibacterial applications: Insights of optoelectrical properties. *Colloid Interface Sci. Commun.* **2021**, *44*, 100467. [CrossRef]
30. Dai, X.; Cui, L.; Yao, L.; Shi, L. Facile construction of novel $Co_3O_4/Bi_{12}O_{17}Cl_2$ heterojunction composites with enhanced photocatalytic performance. *J. Solid State Chem.* **2021**, *297*, 122066. [CrossRef]
31. Li, H.; Hao, X.; Gong, H.; Jin, Z.; Zhao, T. Efficient hydrogen production at a rationally designed $MoSe_2@Co_3O_4$ p-n heterojunction. *J. Solid State Chem.* **2021**, *586*, 84–94. [CrossRef]
32. Xu, X.; Wang, T.; Lu, W.; Dong, L.; Zhang, H.; Miao, X. Co x P@Co_3O_4 Nanocomposite on Cobalt Foam as Efficient Bifunctional Electrocatalysts for Hydrazine-Assisted Hydrogen Production. *ACS Sustain. Chem. Eng.* **2021**, *9*, 4688–4701. [CrossRef]
33. Gao, Z.; Chen, K.; Wang, L.; Bai, B.; Liu, H.; Wang, Q. Aminated flower-like $ZnIn_2S_4$ coupled with benzoic acid modified g-C_3N_4 nanosheets via covalent bonds for ameliorated photocatalytic hydrogen generation. *Appl. Catal. B-Environ.* **2020**, *268*, 118462. [CrossRef]
34. Zhang, Z.; Huang, L.; Zhang, J.; Wang, F.; Xie, Y.; Shang, X.; Gu, Y.; Zhao, H.; Wang, X. In Situ constructing interfacial contact $MoS_2/ZnIn_2S_4$ heterostructure for enhancing solar photocatalytic hydrogen evolution. *Appl. Catal. B-Environ.* **2018**, *233*, 112–119. [CrossRef]
35. Zhang, X.; Chen, Z.; Luo, Y.; Han, X.; Jiang, Q.; Zhou, T.; Yang, H.; Hu, J. Construction of NH_2-MIL-125(Ti)/CdS Z-scheme heterojunction for efficient photocatalytic H_2 evolution. *J. Hazard. Mater.* **2021**, *405*, 124128. [CrossRef] [PubMed]
36. Chen, Z.; Pan, J.; Mei, J.; Yu, Q.; Wang, P.; Wang, P.; Wang, J.; Song, C.; Zheng, Y.; Li, C. Ternary Co_3O_4/CdS/$SrTiO_3$ core-shell pn junctions toward enhanced photocatalytic hydrogen production activity. *J. Environ. Chem. Eng.* **2021**, *9*, 104895. [CrossRef]
37. Jiang, H.; Xing, Z.; Zhao, T.; Yang, Z.; Wang, K.; Li, Z.; Yang, S.; Xie, L.; Zhou, W. Plasmon Ag nanoparticle/Bi_2S_3 ultrathin nanobelt/oxygen-doped flower-like MoS_2 nanosphere ternary heterojunctions for promoting charge separation and enhancing solar-driven photothermal and photocatalytic performances. *Appl. Catal. B-Environ.* **2020**, *274*, 118947. [CrossRef]
38. Poudel, M.B.; Ojha, G.P.; A kim, A.; Kim, H.J. Manganese-doped tungsten disulfide microcones as binder-free electrode for high performance asymmetric supercapacitor. *J. Energy Storage* **2022**, *47*, 103674. [CrossRef]
39. Lin, B.; Li, H.; An, H.; Hao, W.; Wei, J.; Dai, Y.; Ma, C.; Yang, G. Preparation of 2D/2D g-C_3N_4 nanosheet@$ZnIn_2S_4$ nanoleaf heterojunctions with well-designed high-speed charge transfer nanochannels towards high-efficiency photocatalytic hy-drogen evolution. *Appl. Catal. B Environ.* **2018**, *220*, 542–552. [CrossRef]
40. Gao, Y.; Lin, H.; Zhang, S.; Li, Z. Co$(dmgH)_2$pyCl as a noble-metal-free co-catalyst for highly efficient photocatalytic hydrogen evolution over hexagonal $ZnIn_2S_4$. *RSC Adv.* **2016**, *6*, 6072–6076. [CrossRef]
41. Li, Q.; Cui, C.; Meng, H.; Yu, J. Visible-light photocatalytic hydrogen production activity of $ZnIn_2S_4$ microspheres using carbon quantum dots and platinum as dual co-catalysts. *Chem. Asian. J.* **2014**, *9*, 1766–1770. [CrossRef] [PubMed]
42. Huang, T.; Chen, W.; Liu, T.; Hao, Q.; Liu, X. $ZnIn_2S_4$ hybrid with MoS_2: A non-noble metal photocatalyst with efficient photocatalytic activity for hydrogen evolution. *Powder Technol.* **2017**, *315*, 157–162. [CrossRef]
43. Mei, Z.; Ouyang, S.; Tang, D.; Kako, T.; Golberg, D.; Ye, J. An ion-exchange route for the synthesis of hierarchical $In_2S_3/ZnIn_2S_4$ bulk composite and its photocatalytic activity under visible-light irradiation. *Dalton Trans.* **2013**, *42*, 2687–2690. [CrossRef] [PubMed]
44. Chen, Y.; Tian, G.; Zhou, W.; Xiao, Y.; Wang, J.; Zhang, X.; Fu, H. Enhanced photo- generated carrier separation in CdS quantum dot sensitized $ZnFe_2O_4/ZnIn_2S_4$ nanosheet stereoscopic films for exceptional visible light photocatalytic H_2 evo-lution performance. *Nanoscale* **2017**, *9*, 5912–5921. [CrossRef] [PubMed]